Nanoscale

Defect dynamics in two-dimensional black phosphorus under argon ion irradiation

Journal:	*Nanoscale*
Manuscript ID	NR-ART-01-2021-000567.R1
Article Type:	Paper
Date Submitted by the Author:	19-Apr-2021
Complete List of Authors:	Gupta, Saransh; University of Louisville, Department of Mechanical Engineering Periasamy, Prakash; Lam Research Corp Narayanan, Badri; University of Louisville, Department of Mechanical Engineering

Defect dynamics in two-dimensional black phosphorus under argon ion irradiation

Saransh Gupta[1], Prakash Periasamy[2] and Badri Narayanan[1*]

[1]Department of Mechanical Engineering, University of Louisville, Louisville KY 40223, USA

[2]Lam Research Inc., Fremont, CA 94538, USA

Abstract:

Fundamental understanding of the atomic-scale mechanisms underlying production, accumulation, and temporal evolution of defects in phosphorene during noble-gas ion irradiation is crucial to design efficient defect engineering routes to fabricate next-generation materials for energy technologies. Here, we employed classical molecular dynamics (CMD) simulations using a reactive force field to unravel the effect of defect dynamics on the structural changes in a monolayer of phosphorene induced by argon-ion irradiation, and its subsequent relaxation during post-radiation annealing treatment. Analysis of our CMD trajectories using unsupervised machine learning methods showed that radiation fluence strongly influences the type of defects that form, their dynamics, as well as their relaxation mechanisms during subsequent annealing. Low ion fluences yielded a largely crystalline sheet featuring isolated small voids (up to 2 nm), Stone-Wales defects, and mono-/di-vacancies; while large nanopores (~10 nm) can form beyond a critical fluence of ~10^{14} ions/cm^2. During post-radiation annealing, we found two distinct relaxation mechanisms, depending on the fluence level. The isolated small voids (1-2 nm) formed at low ion-fluences heal *via* local re-arrangement of rings, which is facilitated by a cooperative mechanism involving a series of atomic motions that include thermal rippling, bond formation, bond rotation, angle bending and dihedral twisting. On the other hand, damaged structures obtained at high fluences exhibit pronounced coalescence of nanopores mediated by a mechanism involving formation of 3D networks of P-centered tetrahedra. These findings provide new perspectives to use ion beams to precisely control the concentration and distribution of specific defect types in phosphorene for emerging applications in electronics, batteries, sensing, and neuromorphic computing.

*Corresponding author, Email: badri.narayanan@louisville.edu

Keywords: ion bombardment, molecular dynamics, phosphorene, defect dynamics

1. Introduction

Controlled introduction of structural defects, such as point imperfections (e.g., vacancies,), topological irregularities (e.g., Stone-Wales), extended lines (e.g., boundaries), and nanopores, has emerged as a powerful route to achieve several key technology-relevant functionalities in two-dimensional (2D) materials.[1-5] Numerous approaches have been proposed for such precise engineering of defects in 2D materials, including irradiation with ions or electrons,[6, 7] exposure to ultraviolet light[8], chemical doping[9], and plasma treatment.[10, 11] Of these, irradiation of 2D monolayers with energetic ions or electrons has been exceedingly popular owing to its ease of operation, and good control over regions of exposure.[3, 5, 12, 13] Importantly, ion/electron irradiation has enabled novel chemical, opto-electronic, magnetic, and ion-transport behavior in graphene,[2, 3, 5, 14] transition metal di-chalcogenides (TMDs),[15-20] hexagonal boron nitride (*h*-BN),[21-24] and other 2D materials.[13, 25] For instance, bombarding graphene with beams of swift heavy ions (e.g., gallium) yields sub-nanometer pores with excellent selectivity for ion-transport making them suitable for desalination of water, chemical separation, and water purification.[14, 26] Similarly, ion-radiation has been successfully employed to fabricate defective 2D TMD structures, which exhibit improved electron transport in field effect transistors,[18] increased stiffness,[15] excellent magnetic ordering,[17] and enhanced visible photoluminescence;[16, 27] additionally, optoelectronic properties of *h*-BN monolayers and other emerging 2D materials can be modulated effectively using ion/electron irradiation.[13, 21-25]

In recent times, monolayer of black phosphorous (or phosphorene) has attracted a lot of attention due to its unique puckered structure, and the consequent remarkable in-plane anisotropy in its mechanical, thermal, and opto-electronic properties.[28-31] In particular, the lower symmetry structure of phosphorene (as compared to graphene and TMDs) underlies thickness-dependent electronic band gap (1.5 eV in monolayer to 0.3 eV in bulk[29]), high hole mobility[29] ($\sim 10^5$ $cm^2/V/s$), large drain current modulation,[28] negative Poisson ratio,[32] selective adsorption of gases,[33] and excellent optical properties in phosphorene.[34] Such unique combination of physical properties makes phosphorene lucrative for use in field effect transistors, nano-mechanics, gas sensors, photonic devices, and photovoltaic junction thin-film solar cells.[28, 29, 31-33, 35, 36] From the perspective of defect engineering, the relatively weak P–P bonding, rich variety of possible

hybridization states for P atom, and variable atomic coordination around P (up to 6 neighbors) enables (a) high structural flexibility, (b) low vacancy formation energy resulting in high vacancy concentration at room temperature, (c) fast vacancy migration even under ambient conditions, and (d) highly anisotropy in migration of single vacancies (SVs) with SV hopping rates in zigzag direction three orders of magnitude greater than that along armchair direction.[37-39] These properties enable a much wider variety of defect configurations in phosphorene than that observed in other mono-atomic 2D materials, such as graphene and silicene.[40] For instance, several defect configurations, such as a reconstructed 4|10|4 double vacancy featuring a 10-member P-ring sandwiched between two 4-member P-rings and line boundary phases containing tetrahedrally coordinated P atoms, are observed only in phosphorene; these do not exist in graphene and silicene.[40] Such defects have been reported to introduce novel functionalities in phosphorene, including hole-doping,[40] semi-metallicity,[13] local magnetic moments,[40] improved activity for hydrogen evolution reactions,[41, 42] enhanced ion-transport for alkali-ion batteries,[43] and unique photo-responses for emerging applications in neuromorphic computing.[44, 45] Importantly, recent reports have successfully demonstrated that these structural defects can be introduced in phosphorene by irradiating it with energetic particles.[13, 39] This opens up a unique opportunity to design next-generation functional materials *via* defect engineering of phosphorene using ion beams.

Most of the emerging applications in electronics (e.g., neuromorphic devices), battery anodes, and gas sensing require phosphorene sheets with a prescribed density and distribution of specific types of defects (e.g., vacancies, nanopores etc.).[25, 43-45] Such a precise control over the concentration and spatial arrangement of defects in phosphorene under ion-beams remains exceedingly difficult; this, in turn, has thwarted defect engineering in phosphorene. The challenge primarily stems from a lack of fundamental understanding of the atomic-scale processes underlying generation, accumulation, and temporal evolution of various types of defects under ion irradiation of phosphorene. Until now, efforts on characterizing response of phosphorene to irradiation have been largely limited to impacts from energetic electron beams using first principles simulations and *in situ* electron microscopy.[13, 39] Even for electrons, previous works have focused primarily on characterizing the structure of various defects (e.g., single-vacancies, di-vacancies, Stone-Wales etc.), their formation energetics, their migration kinetics, and electronic properties.[13, 39] In particular, recent *ab initio* molecular dynamics (AIMD) studies of isolated collision events

showed that displacement threshold energies for primary knock-on damage in phosphorene are quite low, and that electron beams can be used to fabricate isolated zig-zag atomic chains with semi-metallic character.[13, 39] Furthermore, density functional theory (DFT) calculations predict that formation energy of single-vacancy in phosphorene (1.65 eV) is much lower than that in graphene (7.57 eV);[38] this is consistent with previous scanning tunning microscopy reports of abundance of single-vacancies in phosphorene.[46] More recently, combination of *in situ* transmission electron microscopy and DFT calculations revealed atomic-scale pathway for migration of a di-vacancy, and elucidated aggregation of single, di-, and tri-vacancies into vacancy lines.[39] Despite these recent successes, the atomistic details of the dynamical events associated with nucleation of defects, interaction between the different defects, and the temporal evolution of morphology of phosphorene sheets under multiple successive ion impacts are still unclear. Such knowledge is urgently needed to design phosphorene-based materials for emerging applications in nano-electronics, batteries, and sensing.[25, 43-45]

Classical molecular dynamics (CMD) simulations based on analytical potentials is an established tool to gain insights into the atomic-scale processes that occur under focused ion-beam irradiation and post-radiation annealing treatments. Previously, this tool has been successfully utilized to characterize radiation damage and explore radiation-tolerance mechanisms in metals, semiconductors, ceramics and 2D materials.[47-51] A comprehensive review of the various CMD techniques employed to study radiation effects on materials is available elsewhere.[52] Of particular relevance to 2D materials, these techniques have been extensively used to elucidate the effect of reduced dimensionality of graphene,[53] MoS_2[12, 54] and other 2D materials[24] on formation of defects during ion-irradiation, and the atomic-scale dynamics associated with their relaxation upon subsequent annealing; no report on CMD simulations of ion-bombardment of phosphorene is available in the literature.

Here, we employ CMD simulations within the framework of a reactive force field[55] to characterize the structural damage in phosphorene induced by ion-radiation and identify key atomic-scale dynamical processes that occur in response to ion-radiation. Using an energetic beam of argon (Ar) as a representative bombarding noble gas ion source, we systematically investigate the effect of ion-radiation fluence on (a) type of defects generated, (b) spatial distribution of defects, and (c) evolution of defects, during radiation and subsequent annealing treatment. We find that fluence amount strongly impacts type of defect generated and accumulated during radiation,

as well as the structural relaxation mechanisms during post-radiation annealing. At low fluences of Ar irradiation, the damaged sheet retains its crystallinity, and features mainly isolated point defects, small voids, and topological Stone-Wales defects. Upon annealing, the small voids completely heal by a mechanism involving local re-organization of rings enabled by the collective effect of thermal rippling, bond formation, bond rotation, angle bending, and dihedral twisting. On the other hand, bombarding phosphorene at high fluences results in large nanopores owing to pronounced sputtering of the phosphorus atoms. These large nanopores further coalesce with each other by a mechanism mediated by formation of 3D networks of P-centered tetrahedra.

2. Methods

We perform CMD simulations using the LAMMPS package[56] to study the response of monolayer (ML) of phosphorene to argon (Ar) ion-bombardment. Several previous CMD studies have successfully characterized structural damage in ion-irradiated materials using a combination of bond-order interatomic potentials (e.g., Tersoff, AIREBO etc.), and universal Ziegler-Biersack-Littmark (ZBL) repulsive potential[57] to describe atomic interactions.[12, 54, 58-60] The bond-order potentials describe defect dynamics within the irradiated material, while ZBL potential accounts for nuclear repulsions at short distances (< 1 Å) between bombarding ions (such as Ar) and the atoms in the irradiated material.[12, 54, 58-60] For investigations of multiple ion impacts, the dispersive interactions between the noble gas ions are typically described using a Lennard Jones (LJ) potential.[54] Motivated by the successes of these previous works,[12, 54, 58-60] we adopted a similar approach using a combination of (a) a general bond-order based reactive force field (ReaxFF)[55, 61] for P-P interactions, which is known to accurately describe formation and dissociation of chemical bonds in a wide range of material systems,[61-63] (b) a purely repulsive Ziegler-Biersack-Littmark (ZBL) potential for Ar-P interactions, and (c) Lennard Jones (LJ) potential to treat the dispersive Ar-Ar interactions.

In the framework of ReaxFF, the total energy of the system is expressed as the sum of contributions from (a) several short-range interactions (including bond stretching, angle bending, dihedral twisting, and over/under coordination) that depend on instantaneous connectivity between atoms, as well as (b) long-range dispersion and electrostatic effects.[62, 64] At a given instant, all the connectivity-dependent (short-range) interactions are functions of bond-orders that are derived from interatomic distances. Importantly, the bond-order between a pair of atoms is strongly

influenced by the local atomic-coordination environment, and thereby, captures many-body effects. Long range van der Waals and Coulomb interactions are accounted for every pair of atoms regardless of their connectivity. The evolution of atomic charges with time is determined using electronegativity equalization method; this, in conjunction with the bond-order concept allows ReaxFF to describe metallic, ionic, covalent, and low-dimensional systems equally well.[49, 61, 62, 64, 65] More importantly, ReaxFF has been successfully employed to investigate defect evolution in graphene under ion bombardment.[61] The ReaxFF parameters used in this study were specifically developed to accurately capture thermodynamic, structural, mechanical, and thermal properties of pristine and defective phosphorene sheets.[55] More relevant to this study, ReaxFF has been reported to be the best available interatomic potential to investigate energetic and dynamical behavior of defects in ML-phosphorene.[55] Other non-reactive potentials available in the literature for phosphorene cannot treat defects accurately. For instance, the Stillinger-Weber potential severely underestimates defect formation energies; in fact, it cannot distinguish the energetic difference between a Stone-Waals defect and pristine phosphorene. On the other hand, the bond-order formalism of ReaxFF enables it to accurately capture relative stability, formation energies, and geometry of defects in ML-phosphorene in excellent accordance with DFT calculations.[55] Formation energy for single-vacancy (SV) and double-vacancy (DV) defects in ML-phosphorene predicted by ReaxFF are in excellent agreement with DFT calculations (within ~8%).[55] Note that the ReaxFF overestimates the formation energy of Stone-Wales (SW) defect in ML-phosphorene by ~36%.[55] Apart from defect energetics, another key property relevant for defect production under ion bombardment is the displacement threshold energy (T_d). This property is defined as the minimum kinetic energy that must be transferred to an atom to permanently displace it from its lattice site and cause structural damage. Using CMD simulations, we found that ReaxFF predicts T_d for P in ML-phosphorene as ~6.5 eV (Supplementary Information, Section S1, Figures S1-S2); which are close to the results obtained by previous AIMD simulations (~6 eV).[13] Such close agreement between ReaxFF and first-principles calculations suggests that the ReaxFF approach should provide good quantitative description of defect production under ion bombardment.

The interactions between the Ar and P atoms are modeled using a universal purely repulsive ZBL potential,[57] which is well-documented to provide a good description of nuclear repulsion at short interatomic distances (below around 1 Å), such as those typically encountered in ion radiation. ZBL has been long been accepted as the standard approach to treat repulsion between

colliding atoms in CMD simulations of ion radiation for a wide range of materials.[66-68] Indeed, we found that ZBL captures the interaction energies for Ar and P atoms at short distances well in good agreement with our density functional theory calculations (Supplementary Information, Figure S4). Finally, the interactions between Ar atoms are described using a LJ potential, defined as $E = 4\varepsilon [(\sigma/r)^{12} - (\sigma/r)^{6}]$, where r is the separation distance between the pair of Ar atoms, ε, and σ are independent parameters. We take the values of ε = 0.0103 eV and σ = 3.45 Å for Ar-Ar interactions, which have been successfully used in previous CMD studies of ion-bombardment in two-dimensional MoS_2.[54] Indeed, the binding energy landscape of an Ar-Ar dimer predicted by LJ is in good agreement with our dispersion-corrected DFT (i.e., DFT+D3)[69] calculations (Supplementary Information, Figure S5)

To demonstrate the suitability of the combination of interatomic potentials chosen here for simulating ion-radiation behavior of ML-phosphorene, we calculated the sputtering yield at various kinetic energies (1 eV – 100 keV) of an incident Ar atom using 30,000 short CMD simulations (1 ps) on small supercell of phosphorene consisting of 2,552 atoms (details on methods available in Supporting Information, Section S1). We found that the dependence of the number of sputtered atoms as a function of Ar-ion energy is qualitatively similar to that in other 2D materials (e.g., graphene,[70] MoS_2,[12] and hBN[71]), with maximum sputtering yield of ~7 P atoms at an intermediate Ar energy ~600 eV (Supplementary Information, Figure S3). This provides further validation of the approach used in this work to describe atomic interactions. The Ar sputtering yields for phosphorene (maximum of ~7) are much higher than in graphene (with a maximum yield ~1.2 at Ar energy ~300 eV); [70] such high sputtering yields can be attributed to the substantially weaker binding in phospherene (cohesive energy: –3.48 eV/atom)[13] than graphene (cohesive energy: –7.76 eV/atom)[72].

For our CMD simulations, we use an orthorhombic computational supercell of dimensions ~69.3 nm × 65.1 nm × 5 nm containing 120,000 atoms to simulate a ML of pristine black phosphorus. Periodic boundary conditions are employed in the plane of the monolayer, while fixed boundary conditions are used in the direction normal to the sheet. The ML-phosphorene is first thermalized under ambient conditions (300 K, 1 atm) for 1 ns under isothermal-isobaric conditions (NPT) followed by equilibration for additional 2 ns at 300 K at constant volume using the canonical ensemble (NVT). Constant temperature/pressure conditions are maintained using the Nose-Hoover thermostat/barostat. The thermalized ML-phosphorene exhibits the typical puckered structure with

characteristic P-P bond lengths ~2.23 Å, and bond angles of θ_1 ~100.7° and θ_2 ~103°, in excellent agreement with previous first-principles studies (Figure 1(a,b)).[73, 74] This equilibrated sheet exhibits wrinkling (Supplementary Information, Figure S6), consistent with previous works on other 2D materials.[75]

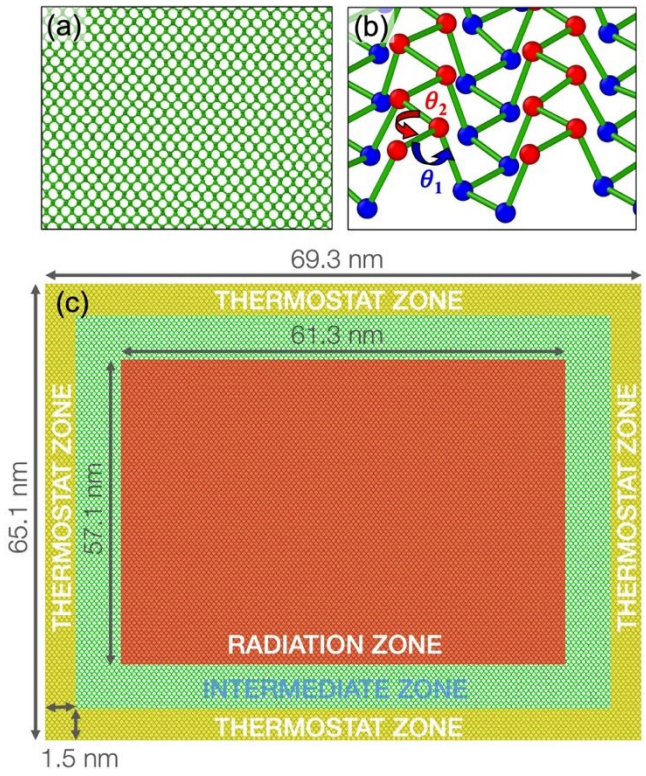

Figure 1. Classical molecular dynamics simulation set-up for argon ion bombardment of monolayer phosphorene. Pristine ML-phosphorene sheet with dimensions 69.3 nm × 65.1 nm (120,000 atoms) is first equilibrated under ambient conditions using CMD simulations within the framework of ReaxFF. Selected regions of the thermalized sheet are shown from two different viewpoints, namely (a) Top, and (b) Side. The top view illustrates that the thermalized sheet contains only six-membered rings of P atoms, while the side view highlights the puckered nature of the sheet, as described by two bond angles θ_1 and θ_2. For the sake of clarity, in panel (b), the atoms belonging to the two different planes in the sheet are depicted by spheres of distinct colors (red: top, blue: bottom). (c) To simulate Ar bombardment, the atoms in the thermalized sheet are classified into three distinct zones by their location, namely radiation (red), intermediate (green), and thermostat (gold). Only the P atoms in the radiation zone are bombarded by high-energy Ar ions; the atoms in the thermostat zone are coupled with Nose-Hoover thermostat held at 300 K to simulate a heat sink. The atoms in the radiation and intermediate zones are treated using a micro-canonical (NVE) ensemble.

Next, we mimic ion-bombardment by introducing Ar atoms at random locations (as implemented by fix deposit in LAMMPS) over a central area of the thermalized phosphorene (61.3 × 57.1 nm^2; 0.75 times total sheet area) called the radiation zone shown by the red region in Figure

1(c). The initial kinetic energy of the newly inserted Ar atoms is set at 25 eV with velocities pointed along arbitrary directions towards the radiation zone, following earlier works on defect engineering of 2D materials via ion-radiation.[76] Previous first principles studies on electron-radiation of phosphorene demonstrate that the kinetic energy chosen in this work is sufficiently low to expect the damage to be caused by nuclear collisions alone. Additionally, effects of charging and electronic excitation are expected to be minimal in phosphorene owing to its small band gap. Therefore, similar to previous CMD studies on ion radiation of 2D materials, we have ignored electronic and charge effects. Note that we do not introduce any initial charge on the incoming argon atom; as typical in the literature of CMD simulations of ion radiation, we refer the incoming neutral argon *atoms* as *ions* analogous to experiments. The atoms located within ~1.5 nm of the edges of the supercell (gold region in Figure 1(c)) are held at ambient temperature (300 K) in the canonical ensemble to simulate a heat sink. The equations of motion for all other atoms are integrated within the microcanonical ensemble to account for the energy deposited by the bombarding ions. Similar approach has been successfully employed to account for heat-dissipation in CMD studies of ion radiation in other 2D materials.[53, 61] An extremely small-time step of 0.005 fs is employed during irradiation to avoid high atomic displacements within a single timestep during the ion-impacts.

Numerous Ar ion fluences in the range $2.86 \times 10^{13} - 1.43 \times 10^{14}$ Ar/cm^2 are simulated. ions These fluences are similar to those used in typical experiments for defect-engineering in two-dimensional materials (10^{12} - 10^{16} ions/cm^2).[76] For any fluence, we employ a dose rate of 2×10^{25} ions/cm^{2}s similar to that used in earlier ion-bombardment studies on graphene (10^{24} to 10^{27} /cm^2.s).[61] The dose rate used in CMD simulations are significantly higher than that in typical experiments due to the limits imposed by computational costs. Note, we ensured that the radiation-induced atomic displacements are significantly far away from the thermostat zone (heat-sink) to avoid any spurious artifacts. After the irradiation is completed up to the desired fluence, the damaged sheet is subjected to a thermal annealing at a higher temperature of 700 K for 5 ns (with a timestep of 0.5 fs) using canonical ensemble. The slightly higher temperature is necessary to sufficiently accelerate the defect dynamics to capture the complete reconstruction of defects within CMD timescales.

3. Results and discussion

We first analyzed our large-scale ReaxFF-CMD trajectories to understand the influence of radiation fluence (10^{13}-10^{14} Ar ions/cm^2) on the structural damage caused by ion impacts in ML-phosphorene, and its relaxation during subsequent annealing (Figure 2). In pristine ML-phosphorene equilibrated under ambient conditions, each P atom is surrounded by three other P neighbors at a distance of ~2.3 Å in a puckered honeycomb lattice structure (Figure 1(a)), consistent with previous reports.[40, 77, 78] Upon Ar-ion bombardment, a significant fraction of the P atoms lose their 3-fold coordination resulting in P atoms coordinated with 2 or 4 P neighbors (Figure 2(a-c)). As expected, the fraction of the over-/under-coordinated P atoms increases progressively with radiation fluence. For instance, at low ion fluence of 2.86×10^{13} Ar/cm^2, only ~3% of the P atoms lose their 3-fold coordination, while increasing the fluence to 1.43×10^{14} Ar/cm^2 disrupts the ideal coordination around ~18% P atoms (Figure 2(a-c)). Direct visualization of the CMD snapshots clearly shows that over-/under-coordinated P atoms occur predominantly at the edges of holes and nanopores formed due to sputtering of P atoms by impacting Ar ions (Figure 2(d-f)). We also observed a few one-dimensional zig-zag chains of P atoms at high fluences (coordination number of 2), akin to those reported in a recent DFT study on electron-beam induced defects in phosphorene (see for example inset in Figure 2(h)).[13] Similar under-coordinated configurations (i.e., containing 2-fold atoms) are well-documented to occur at the edges of nanopores in graphene, h-BN, MoS_2 and other 2D materials under Ar-bombardment.[53, 61]

Typically, over-coordination (such as local tetrahedral arrangement) is a rare occurrence in Ar-irradiated 2D materials, even at higher ion-fluences than that used in the current study. Remarkably, the excellent flexibility of P-P-P bond angles facilitates the formation of 4-fold P-atoms in Ar-irradiated phosphorene (Figure 2(a-c)). Indeed, the average bond lengths (~2.29 Å) and bond angles (~108.75°) around the 4-fold P atoms in our CMD snapshots of irradiated phosphorene sheets are in close agreement to previous reports on allotropes of phosphorene featuring tetrahedral coordination.[55, 79, 80] Such tetrahedrally coordinated P atoms have also been reported to occur in vacancy ad atom defect complexes in electron-irradiated phosphorene,[13] as well as in line-boundary phases in epitaxially grown phosphorene.[81]

The relative fraction of P atoms with 2-, and 4-fold coordination in the irradiated sheet is strongly influenced by the amount of fluence, which in turn, leads to distinct structural morphology

at different fluence levels. At low ion fluence (2.86×10^{13} Ar/cm^2), the irradiated sheet is largely composed of 3-fold P atoms, with small fractions of 2-fold (~2%) and 4-fold (~1%) P atoms. This results in a structure with isolated vacancies, and small voids whose largest dimension is < 2 nm as shown in Figure 2(d). On the other hand, as the radiation fluence increases, the relative fraction of 4-fold P-atoms increases appreciably (Figure 2(a-c)). Indeed, at 1.43×10^{14} Ar/cm^2, the fractions of 3-fold, 2-fold, and 4-fold P atoms are ~82%, ~7% and ~11%; this results in large nanopores (~10 nm), whose edges are stabilized by tetrahedrally coordinated P-atoms (Figure 2(h)).

Interestingly, the irradiated structures at various fluence levels show marked differences in their relaxation behavior upon subsequent thermal annealing at 700 K. The small, isolated voids formed at low fluence (< 2.86×10^{13} Ar/cm^2) heal almost completely to form coherent (albeit defective) lattice *via* local reconstruction into various topological defects such as Stone-Wales (SW), single and divacancy (Figure 2(c)). As a case in point, the insets in Figures 2(b,c) illustrate the healing of a representative small isolated void *via* formation of a stable 5-77-5 SW defect. Such local reconstructions eliminate void edges, causing more than half the 2-fold P-atoms to regain their ideal coordination (3-fold) during annealing (Figure 2(a)). The 4-fold P-atoms also revert back to 3-fold coordination, albeit to a lesser degree (~16%); the remnant 4-fold P-atoms coexist with the topological defects (Figure 2(g)). On the other hand, large nanopores present in the irradiated sheet at high fluence (> 1.43×10^{14} Ar/cm^2) tend to coalesce with each other (Figure 2(f,i) and the insets). This coalescence of the voids is associated with an appreciable increase in the number of tetrahedral P-atoms (~9%) (Figure 2(c)). Direct visualization of the RMD trajectory shows that these new tetrahedral P-atoms form a 3D network around the edges of the large nanopores (Figure 2(f) inset). Such 3D networks thwart the recovery of local coordination around the edge P atoms, even upon annealing for a long time (Figure 2(i) inset). In the intermediate fluence regime (e.g., 8.57×10^{13} Ar/cm^2), we observe that many voids are sufficiently large to heal *via* ring re-organization. At the same time, the voids do not coalescence upon annealing; the shapes of the voids change slightly. Note that a few small voids appear in the sheet irradiated at intermediate fluence, which heal during annealing.

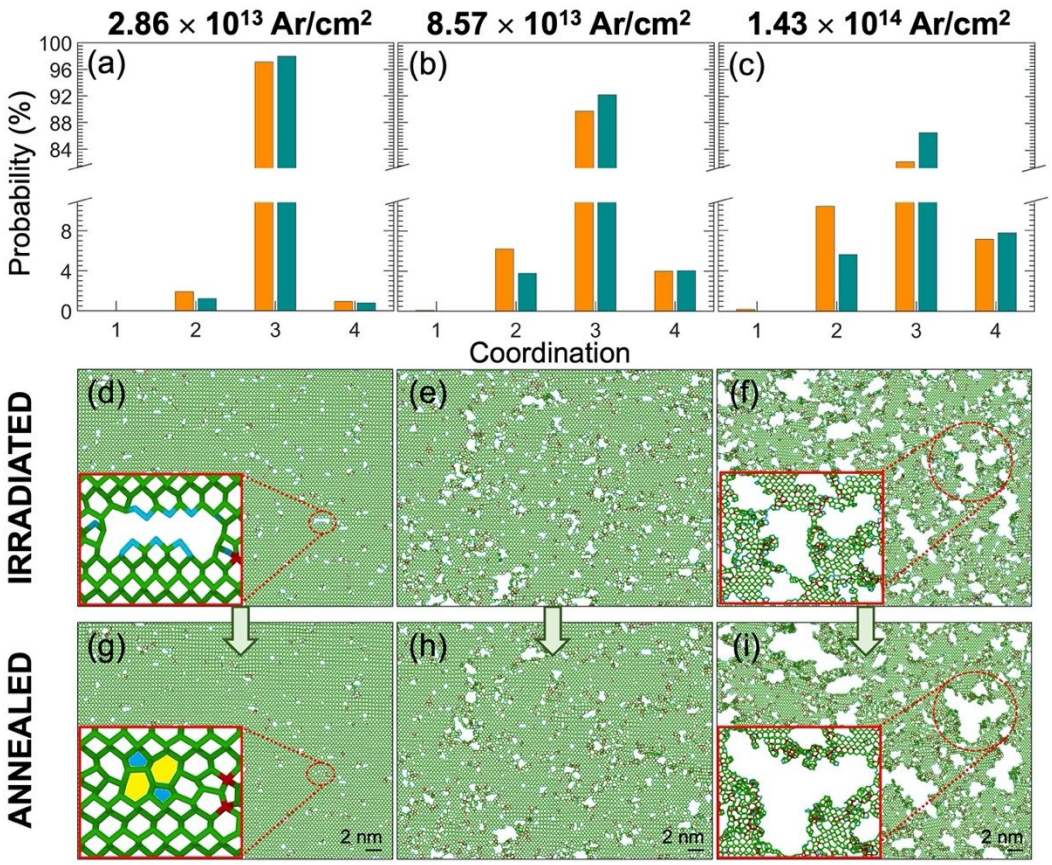

Figure 2. Characterization of structural damage in ML-phosphorene caused by Ar ion bombardment and its relaxation during subsequent annealing at 700 K. To provide a measure of radiation-induced changes in short-range structural order of phosphorene, we calculate the relative fraction of P atoms with different coordination in the sheets after irradiation (orange) and at the end of the subsequent annealing (green) at 700 K for 5 ns for three representative fluence levels, namely (a) 2.86×10^{13} Ar/cm^2, (b) 8.57×10^{13} Ar/cm^2, and (c) 1.43×10^{14} Ar/cm^2. Selected regions in the atomic snapshots after (d-f) irradiation and (g-i) annealing obtained from our ReaxFF-MD simulations are shown for the three fluences, 2.86×10^{13} Ar/cm^2 [panels (d,g)], 8.57×10^{13} Ar/cm^2 [panels (e,h)], and 1.43×10^{14} Ar/cm^2 [panels (f,i)]. The sheets irradiated at low Ar fluence contain small isolated nanopores, which heal via reconstruction of rings upon annealing. A representative nanopore that heals completely is shown in insets of panels (d) and (g). On the other hand, sheets exposed to high Ar fluence feature large nanopores, which coalesce upon annealing; an example is illustrated in the insets of panels (f) and (i).

Figure 3 elucidates the evolution of size distribution of the nanopores (or voids) during ion-bombardment of ML-phosphorene at various fluence levels, and subsequent thermal annealing. We employ an unsupervised machine learning (clustering) method called DBSCAN[82] to identify nanopores of a particular size and obtain a frequency distribution of the sizes in a fast and automatic manner. In this method, the RMD snapshot of interest is first voxelized using a grid of

size 1.5 Å × 1.5 Å × 50 Å, and all empty voxels (i.e., vacancy) are marked. Thereafter, we employ a local density-based clustering algorithm DBSCAN to assign each vacant voxel to a neighboring group of vacancies (i.e., a nanopore) if it has a minimum of 6 neighboring vacant voxels within 2.2 Å. Details about the DBSCAN method can be found elsewhere.[82] Previously, we had successfully employed this approach to determine pore size distribution in self-assembled metal-organic heterostructures, analyze grain growth in ice, and perform autonomous microstructural characterization in a wide variety of materials. Consistent with direct visualization of our RMD trajectories, DBSCAN-clustering analysis shows that the average nanopore size (as well as the size of the largest nanopore) in the irradiated sheets increases progressively with fluence (Figures 2,3). At low fluences, the irradiated sheet contains uniformly distributed voids with cross-sectional area < 80 Å^2 that are well-separated from each other. Upon annealing, there is a marked reduction in the number of nanopores and a shift in the frequency distribution towards smaller sizes (Figure 3(a)). In fact, most voids heal almost completely, which, in turn, results in ~45% decrease in the overall nanopore area (Figure 3(d)). This clearly demonstrates that morphological evolution of phosphorene irradiated at low fluences is dominated by healing of voids, consistent with findings in Figure 2 (a,d,g).

As the ion fluence is increased to intermediate levels (8.57×10^{13} Ar/cm^2), we observe bigger nanopores (up to 450 Å^2) at the end of bombardment that are well-separated from each other (edge-to-edge distance between closest nanopores is at least 8 Å). The irradiated sheet also featured several small voids which healed via ring reorganization. However, the larger ones (with cross-sectional area > 90 Å2) reduce in size slightly and undergo change in shape via reconstruction around the edges (Figure 3(b)). Overall, upon annealing, the total nanopore reducing by only ~18%, which suggests lower healing than that at low fluences. On the other end, at high fluence (>1.43×10^{14} Ar/cm^2), hundreds of large nanopores form, whose cross-sectional areas are at least 5-10 times greater than that found at low fluences (Figure 3(c)). Interestingly, upon annealing the sheet irradiated under high fluence (1.43×10^{14} Ar/cm^2), new pores at higher area (> 2500 Å^2) form at the expense of pores of size >1000 Å^2 (Figure 3(c)); while the number of pores <1000 Å^2 remain nearly constant. In fact, the largest nanopore formed after annealing (~3446 Å^2) is nearly 45 times the area of the largest nanopore in the irradiated sheet (~77 Å^2) as shown in Figure 3(c). Note that the total nanopore area reduces marginally by ~2.5% during annealing, indicative of

negligible healing (Figure 3(d)). Evidently, coalescence of nanopores is the dominant relaxation mechanism for sheets irradiated at high ion fluences.

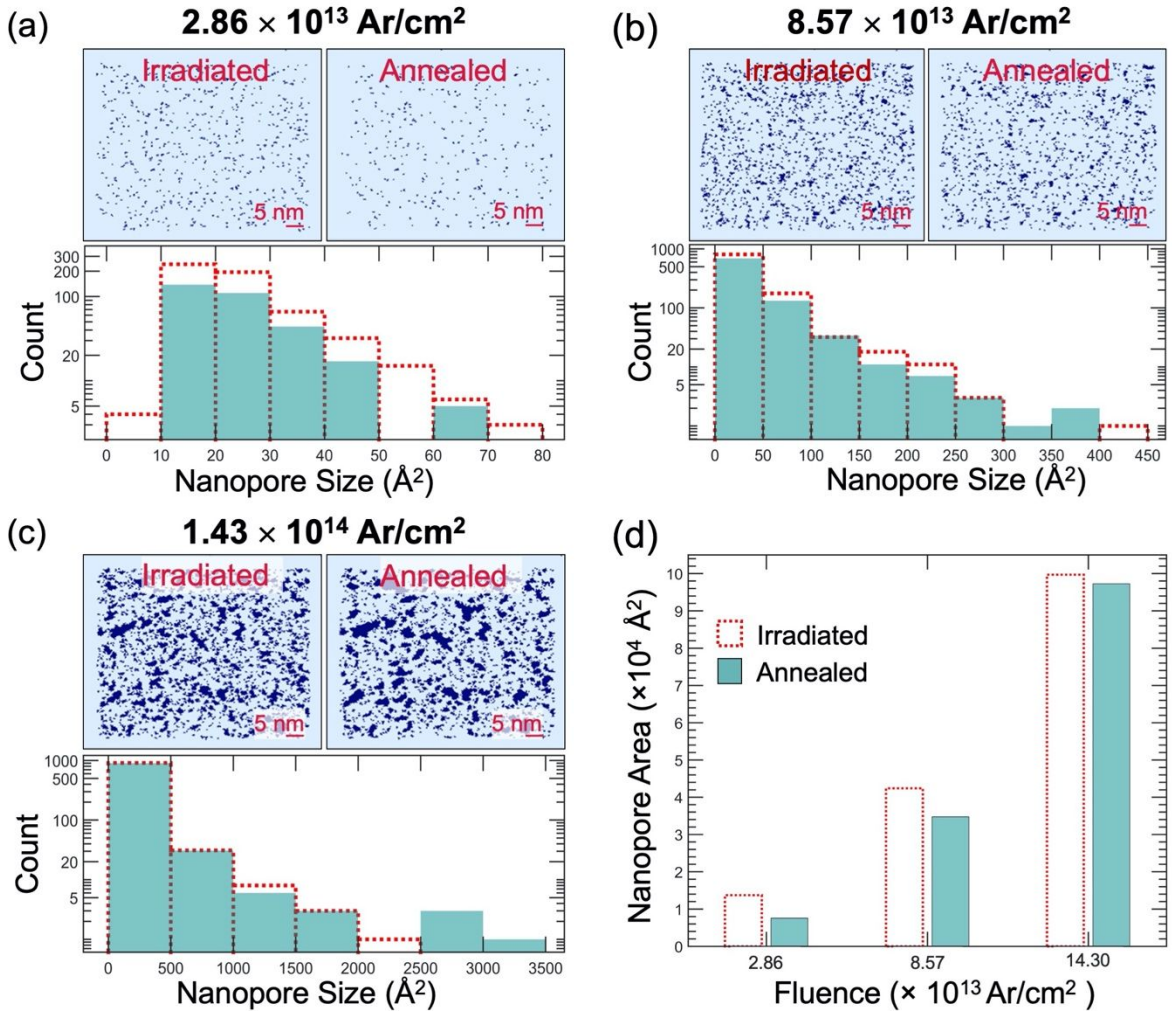

Figure 3. Evolution of nanopores in Ar irradiated ML-phosphorene sheets, as obtained from CMD simulations. Spatial- and size-distribution of nanopores in phosphorene sheet (as identified by DBSCAN clustering algorithm from CMD snapshots) after exposure to Ar irradiation and subsequent annealing at 700 K for three representative fluences levels, namely (a) 2.86 × 10^{13} Ar/cm^2, (b) 8.57 × 10^{13} Ar/cm^2, and (c) 1.43 × 10^{14} Ar/cm^2. (d) Total nanopore area after irradiation and subsequent annealing for different Ar fluences. In panels (a-c), the top view of the sheet after irradiation (top-left) and annealing (top-right) are shown, wherein the nanopores and filled regions are depicted in dark and light blue respectively. The corresponding size distribution of the nanopores (measured by cross-sectional area) are also shown in each panel.

Next, we characterize the radiation-induced structural damage by calculating the integrated radial distribution functions (RDFs), counting the number of P atoms sputtered fom the sheet, as well as quantifying change in crystallinity upon ion bombardment and subsequent annealing

(Figure 4). Integrated RDFs provide an effective visual way to rapidly assess the long-range order of crystals, including 2D monolayers. For pristine phosphorene, integrated RDF (coordination $Z(r)$ as a function of separation distance r) exhibits plateaus at characteristic P-P separation distances that correspond to different neighbor shells (Figure 4(a)). Any disruption in the step-like nature of the $Z(r)$ plot indicates loss of crystallinity. Although integrated RDF provide a quick way to visually assess the structural damage, it does not provide any quantitative insight. To quantitatively assess long-range disorder induced by ion-bombardment, we define crystallinity as the ratio between 6-membered P-rings and the total number of rings in the impacted region. This metric is motivated by previous studies on graphene, wherein fraction of carbon atoms belonging to 6-membered honeycomb rings has been successfully employed as an accurate indicator of crystallinity. Note, this definition will yield 100% crystallinity for a pristine ML of phosphorene, since it is entirely made up of puckered 6-membered P-rings (Figure 1(a)).

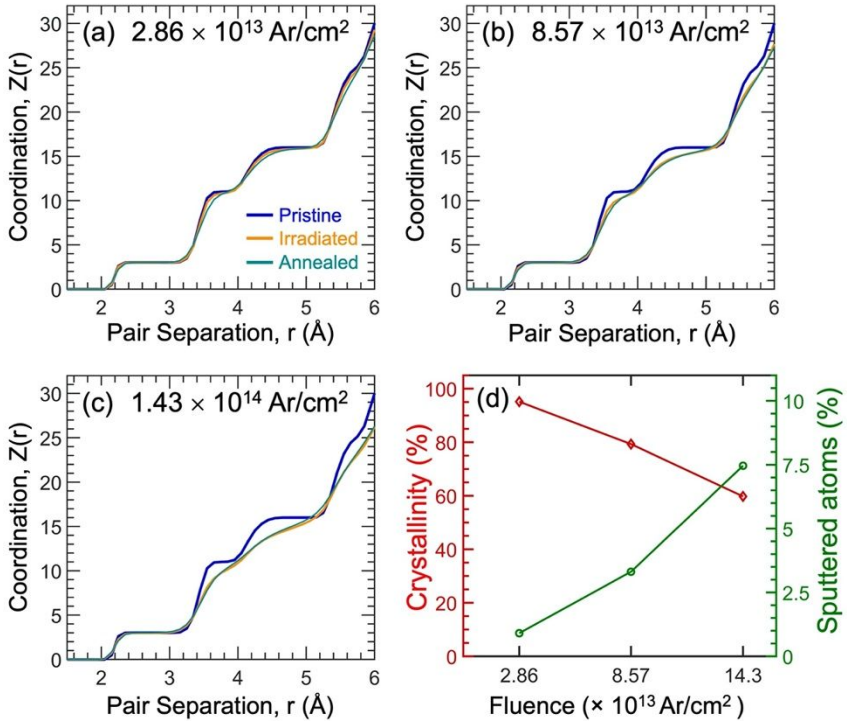

Figure 4. Effect of Ar irradiation on structural order in ML-phosphorene sheets. Number of P neighbors, $Z(r)$ as a function of P-P separation distance r in phosphorene after irradiation and subsequent annealing at 700 K for three Ar fluences namely (a) 2.86×10^{13} Ar/cm^2, (b) 8.57×10^{13} Ar/cm^2, and (c) 1.43×10^{14} Ar/cm^2. (d) Change in crystallinity, defined as the probability of finding 6-membered rings in the impacted region, and fraction of sputtered P atoms for different Ar fluences. In panels (a-c), $Z(r)$ for pristine phosphorene sheet equilibrated under ambient conditions is also shown for comparison.

At low radiation fluence (2.86×10^{13} Ar/cm^2), phosphorene largely retains its crystallinity after ion-bombardment as shown by clear plateaus at characteristic separation distances in the integrated radial distribution function (Figure 4(a)). The slight distortion in the long-range order in irradiated phosphorene is further healed upon subsequent annealing resulting in a ~95% crystalline structure. This behavior is consistent with the extremely low number of sputtered P atoms (~0.7%) at this fluence (Figure 3(d)), and also agrees well with our direct visualization of RMD trajectories (Figure 2(b,c)). Similarly, as expected from our findings in Figures 2 and 3, the number of sputtered P atoms increases progressively with radiation fluence resulting in lower crystallinity, dropping to ~60% at high radiation fluence of 1.43×10^{14} Ar/cm^2 (Figure 4(b-d)). The amorphization of the sheet irradiated at fluences > 8.5×10^{13} Ar/cm^2 is clearly evident in the lack of well-defined coordination plateaus in the integrated RDF beyond the first neighbor at P-P separation distance ~2.4 Å, which shows loss of long-range order (Figure 4(b,c). Furthermore, we found that ~0.8 – 1.4 P atoms get sputtered per Ar impact, which is consistent with our single impact simulations (Supplementary Information, Figure S2).

To gain quantitative insights into the influence of Ar-radiation fluence on defect production, and their annihilation/re-organization during subsequent annealing, we analyze our RMD trajectories to collect statistics on the P-rings of different sizes, as well as topological point defects in ML phosphorene during different stages of Ar-irradiation (Figure 5). As expected from their high crystallinity (Figure 4(a,d)), irradiated sheets at low fluences primarily consist of puckered 6-membered P-rings (~92%), which further increase upon thermal annealing to ~95% (Figure 5(a)). As the Ar fluence increases, the relative fraction of 6-membered rings drops consistent with our structural characterization (Figures 2,4); at the same time, the fraction of non-six-membered rings rises. These non-hexagonal rings play a crucial role in local reconstructions of atomic network around voids to a coherent defective lattice without any under-coordinated atoms.[1] More importantly, such reconstruction can retain the planarity of the sheet when the arrangement of polygons satisfies certain symmetry rules (e.g., 5-77-5 Stone-Wales) or induce local curvatures (e.g., collection of pentagons and hexagons in fullerene).[1] Figure 5(a-c) shows that the fraction of the pentagons (5-membered rings) -- a key constituent of several stable defect configurations -- rises significantly upon thermal annealing (up to ~25% at 1.43×10^{14} Ar/cm^2) at all fluences. Indeed, we observe several stable topological defects consisting of various combinations of polygons[40, 83, 84] in Ar-irradiated phosphorene. Many of the defects found in this study are also

commonly found in the other 2D materials such as graphene[1] and/or silicene.[85] Compared to other 2D-materials, these defects are easier to form in phosphorene due to their lower formation energies, [13, 40, 83, 84] and consequently, have a higher areal density.[40]

Single Vacancy (SV-5|9) is the most dominant type of point defect in the irradiated phosphorene samples regardless of ion fluence (Figure 5(e)), despite its slightly higher formation energy (1.63 – 1.71 eV) than the most stable point defect, i.e., 5|77|5 Stone-Wales (SW) defect (1.01 –1.62 eV).[40, 86, 87] The preferential formation of SVs is due to the high collision cross-section for Ar-irradiation. Essentially, due to the comparable sizes of Ar and P atoms (covalent radii of P: 1.06 Å, Ar: 0.97 Å), the incoming Ar ions are able to transfer large part of their kinetic energy to the phosphorene sheet; this, in turn, causes primary knock-on P atoms to sputter out of the sheet and form vacancies. The local region around a single missing P atom in the phosphorene sheet quickly re-organizes to form an SV-5|9 configuration, which is quite stable (and does not convert into SW-5|77|5). On the other hand, SW-5|77|5 forms in irradiated phosphorene via ring rearrangement around the P atoms that get displaced from their lattice site without being sputtered, such as ad-atom complexes or vacancy-interstitial pairs (Figure S2). Consistent with our findings, previous works show that SVs are prominent in Ar-irradiated graphene as well owing to the high collision cross-section of Ar radiation.[61] This is particularly interesting since the SVs are more energetically unfavorable in graphene as compared to that in phosphorene (difference in formation energies between SV and SW in graphene ~3 eV and phosphorene ~0.5 eV).[40]

Apart from the 5|9 configuration, SV can also exist in 55|66 form in both silicene and graphene.[85] In phosphorene, however, the reported formation energy of SV-55|66 is substantially (~0.37 eV) higher than SV-(5|9),[84] indicating its lower stability. In fact, SV-55|66 is known to reconstruct into SV-5|9 even at ambient temperature.[40, 84] Consistent with these reports, we do not observe any 55|66-SVs in our irradiated or annealed samples. It is interesting to note that the relative population of SV-5|9 is the highest at low fluence (2.86×10^{13} Ar/cm^2); after annealing they increase by ~2.8 times. This is understandable since the low fluences of Ar are unlikely to cause multiple knock-on events in close proximity to each other, which would intuitively favor formation of isolated SVs. Additionally, most small nanopores/voids formed at low fluences heal by reconstructing into SV-5|9 upon annealing. Such SVs have been reported to enhance hole carrier concentration and introduce ferromagnetic character owing to local magnetic moments (~ 1.0 μ_B) induced by dangling bonds.[40, 84, 88] This raises an interesting possibility of using ion-

bombardment to fabricate phosphorene-based magnetic semiconductor devices. At higher fluences, collision cascades from multiple knock-on events interact with each other, yielding larger nanopores, consistent with our findings in Figure 2.

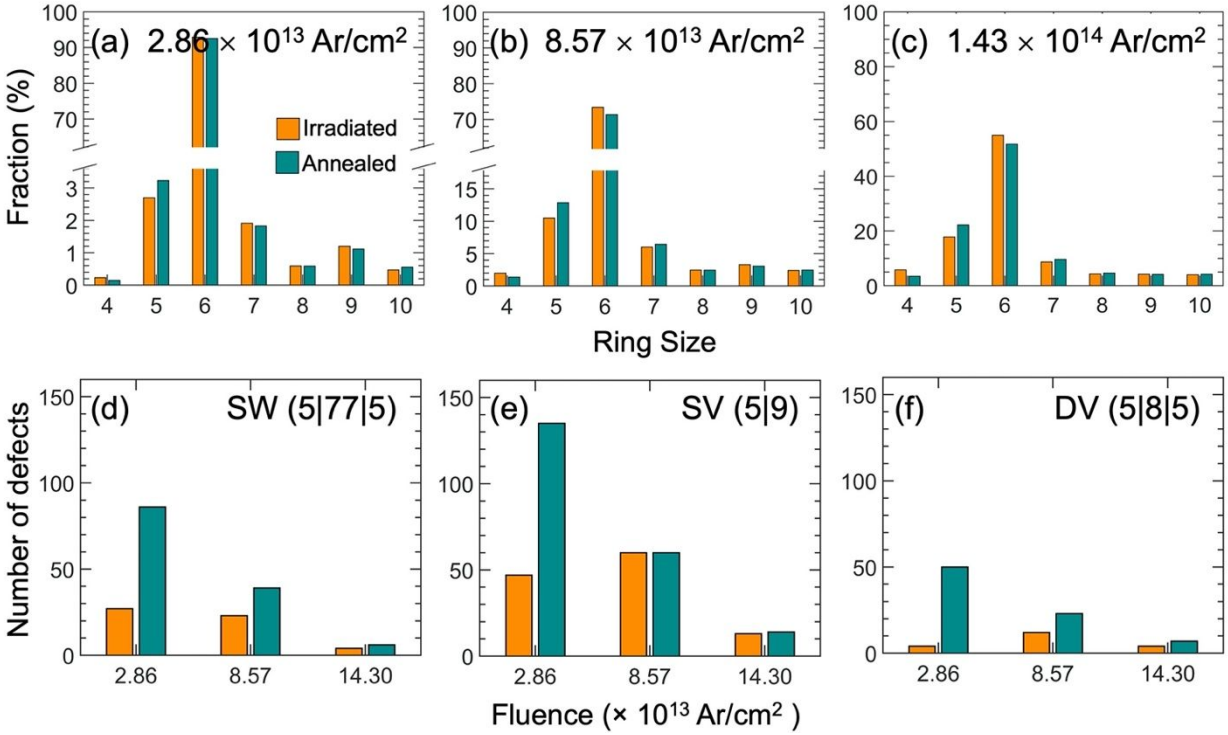

Figure 5. Distribution of defects in ML-phosphorene after Ar bombardment and their dynamical evolution during subsequent annealing at 700 K. Relative population of phosphorus rings of various sizes in phosphorene sheets after irradiation and annealing are shown for three different Ar fluences: (a) 2.86×10^{13} Ar/cm^2, (b) 8.57×10^{13} Ar/cm^2, and (c) 1.43×10^{14} Ar/cm^2. We also analyzed the CMD trajectories to determine the number of (d) Single Vacancy (SV-5|9), (e) Stone-Wales (5|77|5), and (f) Double Vacancy (DV-5|8|5) defects that are generated in the phosphorene sheet at different fluences of Ar radiation, and formed *via* reconstruction during post-radiation annealing treatment at 700 K.

After SVs, the next most populous defect-type in irradiated phosphorene is the most energetically stable Stone-Wales (SW-5|77|5) defect (Figure 5(d)). These defects are self-interstitials that form via 90°-rotation of a P-P bond without creating any P vacancy.[34] They form mostly in regions where the collision cascades lose most of their kinetic energy, and consequently, cannot surpass threshold energy to knock P atoms away from their lattice positions. Their formation is greatly enhanced during the thermal annealing phase, especially, for low fluence cases (2.86×10^{13} Ar/cm^2), where the irradiated sample consists of numerous isolated small voids. These voids undergo atomic reconstruction to form SWs causing a surge in their population, nearly 3

times compared to that in irradiated samples. Importantly, the formation of the SWs preserves the planarity of the sheet with a coherent-yet-defective lattice.

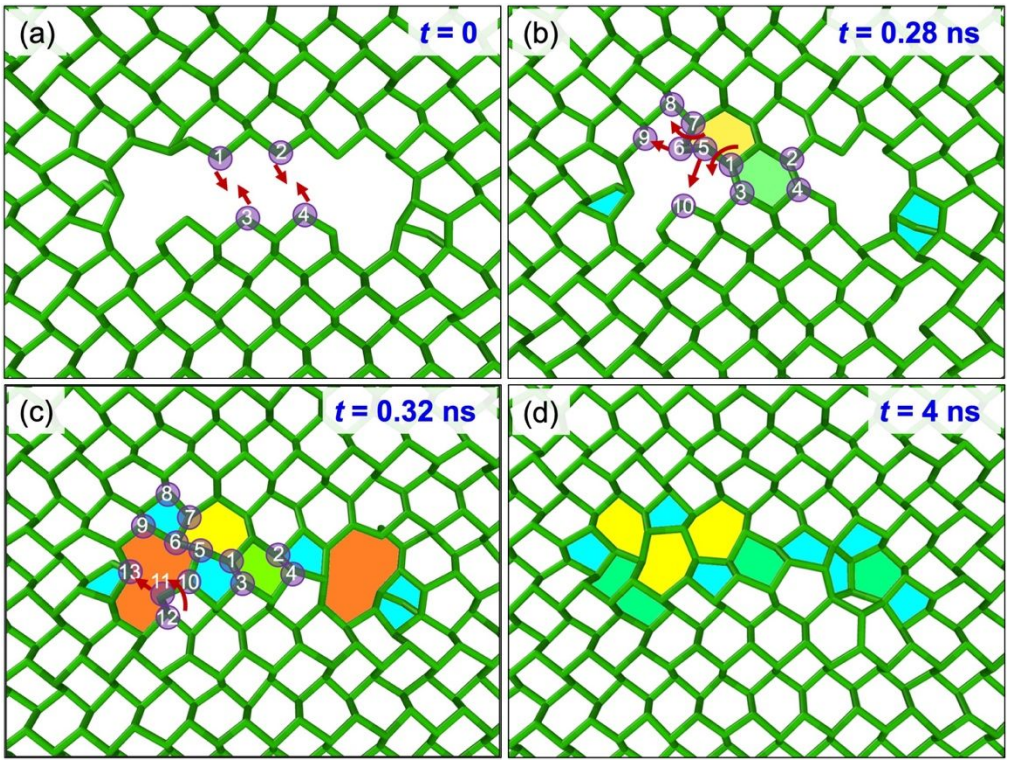

Figure 6. Dynamic processes underlying healing of representative small nanopores formed at low Ar radiation fluences. (a) Atomic snapshot of a representative small nanopore (with smallest dimension ~4 Å), which is generated in the phosphorene sheet exposed to low fluence of Ar radiation (2.86×10^{13} Ar/cm^2). This nanopore heals completely during annealing at 700 K via intermediate steps (b-c) involving a series of local re-arrangement of rings, bond rotation, and formation of new P-P bonds. Such concerted atomic motions eventually result in (d) a coherent network composed of hexagons, pentagons, and SW-5|77|5 defects.

Argon ion bombardment also introduces a divacancy defect, DV-5|8|5[83, 84] in phosphorene at all fluences (Figure 5(f)), whose formation energy is close to SV-5|9.[40, 83, 86] This defect forms when the P atom nearest to a SV gets displaced and the consequent four-dangling bonds reconstruct into a 5-8-5 ring arrangement.[33] SVs are known to exhibit fast hopping rates at room temperature in phosphorene and collide to merge into a DV defect.[39, 86] Localized elevated temperatures near ion-impacts as well as thermal annealing can further enhance the fast diffusion rates of SVs to assist formation of this low-energy stable DV-(5|8|5) defect. This is clearly reflected in the surge of population of DVs upon thermal annealing (~10 times) in lowest fluence case despite their scarcity (~4) in the irradiated structure. The formation of DVs is restricted at higher fluences due to the pre-ponderance of large nanopores. It is worth mentioning that we also observed a few

instance of other known types of divacancy defects, namely DV-4|10|4 and DV-5|7|5|7 at fluences $\geq 8.57 \times 10^{13}$ ions/cm^2; notably, DV-4|10|4 does not form in both graphene and silicene.[40]

Finally, we track the dynamical evolution of the irradiated sheets during thermal annealing at 700 K to identify the atomic scale processes underlying reconstruction of defects. We find that the atomic-scale processes underlying structural evolution during annealing is dictated by the morphology of the irradiated sheet, which, in turn, is determined by the radiation fluence (Figure 2-5). Specifically, our RMD trajectories identify two distinct mechanisms governing relaxation of the structure upon thermal annealing, namely (a) healing of voids via ring-rearrangement, and (b) coalescence of nanopores. Healing of voids *via* ring-rearrangement dominates for sheets irradiated at low Ar^+ fluence (2.86×10^{13} Ar/cm^2), which contain isolated islands of small voids (< 80 Å^2). On the other hand, coalescence of nanopores is more frequent in sheets irradiated at high Ar fluence (1.43×10^{14} Ar/cm^2), where closely spaced large nanopores (> 1000 Å^2) are readily available.

The small, isolated voids present in irradiated sheets at low fluence contain several under-coordinated P atoms along the edges (Figure 2); the closest edge P atoms across these voids can be < 5 Å apart. Upon annealing, these closely located P atoms (a) form new P-P bonds that stitch-up the void (b) recover the ideal P-coordination of 3 and (c) induce a series of ring rearrangements mediated by dihedral rotation around the edges of the voids (Figure 6, Supplementary Movie 1). Such cooperative re-organization causes the voids to reduce in size or heal completely, similar to that observed in graphene. Figure 6 highlights the key atomic-scale dynamical events involved in complete healing of a representative small void ~1.6 nm × 0.4 nm (See Supplementary Movie 1 for the entire trajectory). Initially, in the irradiated sample (at $t = 0$), the void consists of numerous 2-fold coordinated P atoms along the edges (Figure 6(a)), among which two pairs of P atoms, namely 1-3 and 2-4 are separated by ~4 Å. During annealing, the irradiated phosphorene undergoes extensive rippling induced by thermal fluctuations; the extent of rippling is much higher than that observed in graphene, consistent with the lower stiffness of phosphorene as compared to other traditional 2D materials. The pronounced thermal rippling facilitates a wide range of atomic motion, including bond rotation, angle bending and dihedral twisting, particularly near the edge of the voids (Supplementary Movie 1). This random thermal motion causes the 1-3 and 2-4 pairs to eventually come close to each other, within ~2.5 Å at $t \sim 0.25$ ns, resulting in formation of new bonds between 1-3 and 2-4. The newly formed P-P bonds gradually heal over the next 0.05 ns

yielding a separation distance ~2.3 Å, similar to that in pristine phosphorene (Figure 6(b)). Next, we observe significant twisting of two dihedrals, namely 5-6-7-8 and 3-1-5-7 whose dihedra angles change by ~20° (e.g., dihedral angle for 5-6-7-8 changes from ~108° at t = 0.28 ns to ~130° at t = 0.32 ns). Such cooperative twisting allows reduction in the separation distance of two P-P pairs, 6-9 and 5-10 from ~3.5 Å (t = 0.28 ns) to ~2.3 Å (t = 0.32 ns) to form new bonds; and, in turn, enable conversion of a void (with 18 corners) into a combination of two new pentagons and a 11-member ring (Figure 6(c)). Subsequently, twisting of 11-12-10-5 dihedral enables the conversion of this 11-member ring into a heptagon and hexagon via formation of a P-P between the atoms labeled 11 and 13 (Figure 6(d)). A series of such cooperative dihedral twisting and bond formation over the next ~1 ns enables substantial ring re-arrangement to completely heal the void forming a coherent network composed of hexagons, pentagons, and SW-5|77|5 defects. Once formed, this defective coherent network composed of a variety of polygons remains stable, as indicated by the RMD snapshot at t = 4 ns (Figure 6(d)). Our AIMD simulations within the framework of dispersion-corrected DFT (i.e., DFT +D3) show that a small representative hole (with 3 missing P atoms; ~6.7 Å × 4.5 Å) heals to form a coherent network composed of 5--8 membered rings via a similar mechanism involving a series of well-coordinated bond rotation, angle bending, dihedral twisting, and ring re-arrangement motions (Supplementary Movie S2, Section S4, Figure S7). This instills confidence in the long-time healing dynamics illustrated by ReaxFF for small nanopores.

Samples irradiated at high fluences (> 1.43×10^{13} Ar/cm^2) exhibit an entirely different behavior during thermal annealing due to the preponderance of closely spaced large nanopores (> 300 Å^2 in area). In these nanopores, the edge P atoms located at opposite ends are significantly far from each other (at least 1.5 nm), which precludes formation of new P-P bonds that stitch-up the pore. Figure 7 shows the dynamical events that govern the coalescence of two representative neighboring nanopores of sizes ~500 Å^2 (pore 1) and ~950 Å^2 (pore 2) found in phosphorene irradiated at high fluence (1.43×10^{13} Ar/cm^2). The smallest and the largest dimensions of pore 1 are 24 Å and 34 Å respectively; the corresponding sizes for pore 2 are 18 Å and 90 Å. During thermal annealing, the thin region (~7 Å) between two adjoining nanopores undergoes significant reconstruction to form non-planar structures composed of 4-fold P atoms and pentagons (Figure 7(b)). As the annealing proceeds, we observe that the P-centered tetrahedra increase in number at the expense of pentagons and tend to cluster together into disordered 3D aggregates. This, in turn, causes the thin region between pore 1 and pore 2 to roll inwards, which eventually results in merging of the

two nanopores (Figure 7(c), Supplementary Movie S3). Phosphorene morphologies containing such nanopores could be suitable for applications in chemical separations[14, 26].

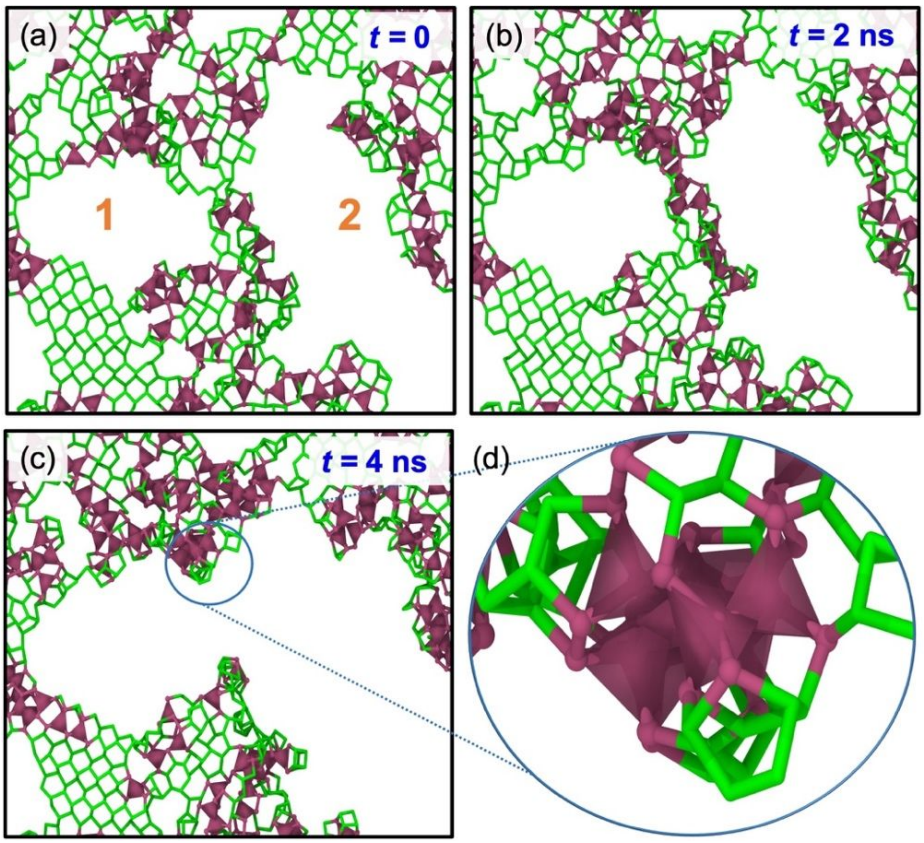

Figure 7. Atomic-scale mechanisms underlying coalescence of large nanopores in irradiated structures at high Ar fluences. (a) Representative snapshot of two large neighboring nanopores (marked as 1 and 2) that form upon exposure to high fluence of Ar irradiation (1.43×10^{14} Ar/cm^2). These nanopores reconstruct via intermediate steps (b-c) involving formation of 3D networks of P_4 tetrahedra (shown in purple) leading to (d) their coalescence.

At intermediate fluences (e.g., 8.57×10^{13} Ar/cm^2), the irradiated sheet features a distribution of defects containing both small voids (< 80 Å^2) and numerous large nanopores (Figure 2,3). The small voids heal *via* mechanism illustrated in Figure 6. We find that the propensity of a void to heal is dictated by its smallest dimension. If the shape of a given void allows for one of the dimensions to be smaller than a critical value of ~5 Å, ring re-arrangement can occur by a cooperative atomic motion involving sheet rippling, bond rotation, angle-bending and dihedral twisting described in Figure 6. Note the size of the other (longer) dimension does not have any impact on healing, e.g., the representative void shown in Figure 6 with dimensions of ~16 Å × ~4 Å heals completely even though the longer dimension is more than thrice the critical value. For

large voids, whose all dimensions are > 6 Å, reconstruction can occur only near the edges; although such reconstructions can reduce the area of the void, it cannot heal the void to completely repair the lattice locally. Also, these large nanopores are sufficiently far apart (edge-to-edge distance between closest voids at least ~8 Å), which precludes the formation of 3D networks of P-centered tetrahedra, necessary to facilitate coalescence. Instead, they just undergo edge reconstruction, which changes their shape and slightly reduces their size. Carefully engineering of the voids formed at intermediate fluence could find applications in quantum dots and other electronic devices[89].

We expect our finding of distinct fluence-dependent mechanisms for relaxation of defective structures during post-radiation annealing (i.e., ring re-arrangement at low fluences, and void coalescence at high fluences) to remain valid for all ion sizes/mass. Although systematic investigations of effect of ion size are beyond the scope of this work, the critical fluence values marking regimes for healing via reorganization of rings or coalescence of nanopores is expected to depend on the size/mass of the bombarding ion. Similarly, size of bombarding ion will certainly impact the relative population of the various defects that form during bombardment. For instance, the significantly smaller size of He as compared to P (covalent radii He: 0.28 Å; P: 1.06 Å) would result in a low radiation cross-section. This, in turn, is expected to result in lower sputtering yield and preferential formation of SW-5|77|5 defects (rather than SV-5|9); similar to previous reports on ion-bombardment of graphene.[61]

Finally, we emphasize that the results reported here are for a free-standing monolayer of phosphorene, such as those suspended on a TEM grid or over a trench in a substrate. In this case, the formation, distribution, and evolution of defects are all primarily governed by direct impact of impinging energetic ions (i.e., argon). The presence of a substrate (e.g., SiO_2) in supported systems introduces additional factors that influence defect production, namely (a) noble gas ions backscattered from substrate, (b) sputtered atoms from the substrate. Additionally, the substrate could limit the motion of sputtered target atoms from the 2D material in the downward direction, which can facilitate recombination of defects (e.g., vacancy-interstitial pairs) and suppress defect formation.[58] Previous CMD/Monte Carlo (MC) simulations of single ion impacts have shown that defect production can be significantly enhanced by backscattered ions and sputtered atoms from the substrate, especially for lighter bombarding ions (e.g., helium).[58] Substrate effects on the defect dynamics in 2D materials under multiple ion impacts remains unclear; and is beyond the scope of

this work. Nevertheless, previous CMD/MC simulations indicate that backscattering is negligible for heavier ions (such as Argon); and the effect of sputtered substrate atoms on the defect production is considerably smaller than the direct Ar impacts. [58] Thus, the results presented in this work for free-standing phosphorene are expected to be relevant for supported systems as well.

4. Conclusions

We employ ReaxFF-CMD simulations to understand the atomic-scale mechanisms that occur in phosphorene in response to ion radiation within the nuclear stopping regime. Using argon as a representative bombarding ion source, we found that ion fluence strongly influences (a) defect production mechanisms, (b) defect dynamics, and (c) nature and concentration of defects accumulated during radiation; as well as (d) structural relaxation during post-radiation annealing treatment. Specifically, we observe that low fluence of Ar irradiation ($< 2.86 \times 10^{13}$ ions/cm^2) yields a fairly ordered planar sheet consisting of isolated small voids, monovacancies, di-vacancies, and extended topological defects (Stone Wales). Upon annealing, most of the small voids healed completely to form a coherent lattice (albeit defective) resulting in a substantial reduction in overall void area (~42%). Our CMD trajectories identify that this healing occurs through re-organization of puckered P rings, which is facilitated by a series of cooperative atomic-scale events including thermal rippling, bond formation, bond rotation, angle bending, and dihedral twisting. The annealed sheet contains isolated monovacancies and Stone Wales defects, which are known to exhibit exciting functionalities, including enhanced hole carrier concentration, ferromagnetism, and improved alkali-ion conduction for batteries. As the fluence increases, the size of the voids increases primarily due to progressively increasing sputtering of phosphorus atoms. At high fluences ($> 1.43 \times 10^{13}$ Ar/cm^2), large nanopores (5-10 nm) form that are sufficiently close to each other (edge-to-edge distance of ~6-7 Å). During annealing, these nanopores coalesce with each other through a mechanism involving formation of 3D networks of P-centered tetrahedra. Finally, at intermediate fluence levels, we find several voids that are both large enough (with all dimensions > 6 Å) to preclude healing via ring reorganization, and sufficiently well-separated (edge-to-edge distance from nearest void > 8 Å) to inhibit coalescence. These findings will provide new perspective to optimize ion-beam engineering of phosphorene based functional 2D materials for applications in nano-electronics, neuromorphic computing, batteries, and gas separation technologies.

Acknowledgements

This work was supported by a gift from Lam Research Foundation and start-up funds at University of Louisville. This research used resources of the National Energy Research Scientific Computing Center, a DOE Office of Science User Facility supported by the Office of Science of the U.S. Department of Energy under Contract No. DE-AC02-05CH11231. Use of the Center for Nanoscale Materials was supported by the U. S. Department of Energy, Office of Science, Office of Basic Energy Sciences, under Contract No. DE-AC02–06CH11357. We also acknowledge the resources at University of Louisville Research Computing Group and Cardinal Research Cluster.

References

1. Banhart, F.; Kotakoski, J.; Krasheninnikov, A. V., Structural Defects in Graphene. *ACS Nano* **2011,** *5* (1), 26-41.
2. Kalbac, M.; Lehtinen, O.; Krasheninnikov, A. V.; Keinonen, J., Ion-Irradiation-Induced Defects in Isotopically-Labeled Two Layered Graphene: Enhanced In-Situ Annealing of the Damage. *Adv. Mater.* **2013,** *25* (7), 1004-1009.
3. Krasheninnikov, A.; Banhart, F., Engineering of nanostructured carbon materials with electron or ion beams. *Nature materials* **2007,** *6* (10), 723-733.
4. Lin, Z.; Carvalho, B. R.; Kahn, E.; Lv, R.; Rao, R.; Terrones, H.; Pimenta, M. A.; Terrones, M., Defect engineering of two-dimensional transition metal dichalcogenides. *2D Materials* **2016,** *3* (2), 022002.
5. López-Polín, G.; Gómez-Navarro, C.; Parente, V.; Guinea, F.; Katsnelson, M. I.; Perez-Murano, F.; Gómez-Herrero, J., Increasing the elastic modulus of graphene by controlled defect creation. *Nature Physics* **2015,** *11* (1), 26-31.
6. Cheng, Z.; Abuzaid, H.; Yu, Y.; Zhang, F.; Li, Y.; Noyce, S. G.; Williams, N. X.; Lin, Y.-C.; Doherty, J. L.; Tao, C., Convergent ion beam alteration of 2D materials and metal-2D interfaces. *2D Materials* **2019,** *6* (3), 034005.
7. Susi, T.; Meyer, J. C.; Kotakoski, J., Quantifying transmission electron microscopy irradiation effects using two-dimensional materials. *Nature Reviews Physics* **2019,** *1* (6), 397-405.
8. Tomašević-Ilić, T.; Jovanović, Đ.; Popov, I.; Fandan, R.; Pedrós, J.; Spasenović, M.; Gajić, R., Reducing sheet resistance of self-assembled transparent graphene films by defect patching and doping with UV/ozone treatment. *Appl. Surf. Sci.* **2018,** *458*, 446-453.
9. Guo, Y.; Xu, K.; Wu, C.; Zhao, J.; Xie, Y., Surface chemical-modification for engineering the intrinsic physical properties of inorganic two-dimensional nanomaterials. *Chem. Soc. Rev.* **2015,** *44* (3), 637-646.
10. Shim, J.; Oh, A.; Kang, D. H.; Oh, S.; Jang, S. K.; Jeon, J.; Jeon, M. H.; Kim, M.; Choi, C.; Lee, J., High-performance 2D rhenium disulfide (ReS2) transistors and photodetectors by oxygen plasma treatment. *Adv. Mater.* **2016,** *28* (32), 6985-6992.
11. Tosun, M.; Chan, L.; Amani, M.; Roy, T.; Ahn, G. H.; Taheri, P.; Carraro, C.; Ager, J. W.; Maboudian, R.; Javey, A., Air-stable n-doping of WSe2 by anion vacancy formation with mild plasma treatment. *ACS nano* **2016,** *10* (7), 6853-6860.

12. Ghorbani-Asl, M.; Kretschmer, S.; Spearot, D. E.; Krasheninnikov, A. V., Two-dimensional MoS2 under ion irradiation: from controlled defect production to electronic structure engineering. *2D Materials* **2017,** *4* (2), 025078.
13. Vierimaa, V.; Krasheninnikov, A. V.; Komsa, H.-P., Phosphorene under electron beam: from monolayer to one-dimensional chains. *Nanoscale* **2016,** *8* (15), 7949-7957.
14. O'Hern, S. C.; Boutilier, M. S.; Idrobo, J.-C.; Song, Y.; Kong, J.; Laoui, T.; Atieh, M.; Karnik, R., Selective ionic transport through tunable subnanometer pores in single-layer graphene membranes. *Nano Lett.* **2014,** *14* (3), 1234-1241.
15. Iberi, V.; Liang, L.; Ievlev, A. V.; Stanford, M. G.; Lin, M.-W.; Li, X.; Mahjouri-Samani, M.; Jesse, S.; Sumpter, B. G.; Kalinin, S. V., Nanoforging single layer MoSe 2 through defect engineering with focused helium ion beams. *Scientific reports* **2016,** *6* (1), 1-9.
16. Jhon, Y. I.; Kim, Y.; Park, J.; Kim, J. H.; Lee, T.; Seo, M.; Jhon, Y. M., Significant Exciton Brightening in Monolayer Tungsten Disulfides via Fluorination: n-Type Gas Sensing Semiconductors. *Adv. Funct. Mater.* **2016,** *26* (42), 7551-7559.
17. Mathew, S.; Gopinadhan, K.; Chan, T.; Yu, X.; Zhan, D.; Cao, L.; Rusydi, A.; Breese, M.; Dhar, S.; Shen, Z., Magnetism in MoS2 induced by proton irradiation. *Appl. Phys. Lett.* **2012,** *101* (10), 102103.
18. Ochedowski, O.; Marinov, K.; Wilbs, G.; Keller, G.; Scheuschner, N.; Severin, D.; Bender, M.; Maultzsch, J.; Tegude, F.; Schleberger, M., Radiation hardness of graphene and MoS2 field effect devices against swift heavy ion irradiation. *J. Appl. Phys.* **2013,** *113* (21), 214306.
19. Patra, T. K.; Zhang, F.; Schulman, D. S.; Chan, H.; Cherukara, M. J.; Terrones, M.; Das, S.; Narayanan, B.; Sankaranarayanan, S. K., Defect dynamics in 2-D MoS2 probed by using machine learning, atomistic simulations, and high-resolution microscopy. *ACS nano* **2018,** *12* (8), 8006-8016.
20. Stanford, M. G.; Pudasaini, P. R.; Belianinov, A.; Cross, N.; Noh, J. H.; Koehler, M. R.; Mandrus, D. G.; Duscher, G.; Rondinone, A. J.; Ivanov, I. N., Focused helium-ion beam irradiation effects on electrical transport properties of few-layer WSe 2: enabling nanoscale direct write homo-junctions. *Scientific reports* **2016,** *6*, 27276.
21. Grosso, G.; Moon, H.; Lienhard, B.; Ali, S.; Efetov, D. K.; Furchi, M. M.; Jarillo-Herrero, P.; Ford, M. J.; Aharonovich, I.; Englund, D., Tunable and high-purity room temperature single-photon emission from atomic defects in hexagonal boron nitride. *Nature communications* **2017,** *8* (1), 1-8.
22. Tran, T. T.; Elbadawi, C.; Totonjian, D.; Lobo, C. J.; Grosso, G.; Moon, H.; Englund, D. R.; Ford, M. J.; Aharonovich, I.; Toth, M., Robust multicolor single photon emission from point defects in hexagonal boron nitride. *ACS nano* **2016,** *10* (8), 7331-7338.
23. Wei, X.; Wang, M.-S.; Bando, Y.; Golberg, D., Electron-beam-induced substitutional carbon doping of boron nitride nanosheets, nanoribbons, and nanotubes. *ACS nano* **2011,** *5* (4), 2916-2922.
24. Zhang, J.; Sun, R.; Ruan, D.; Zhang, M.; Li, Y.; Zhang, K.; Cheng, F.; Wang, Z.; Wang, Z.-M., Point defects in two-dimensional hexagonal boron nitride: A perspective. *J. Appl. Phys.* **2020,** *128* (10), 100902.
25. Kaewmaraya, T.; Ngamwongwan, L.; Moontragoon, P.; Karton, A.; Hussain, T., Drastic improvement in gas-sensing characteristics of phosphorene nanosheets under vacancy defects and elemental functionalization. *The Journal of Physical Chemistry C* **2018,** *122* (35), 20186-20193.

26. Surwade, S. P.; Smirnov, S. N.; Vlassiouk, I. V.; Unocic, R. R.; Veith, G. M.; Dai, S.; Mahurin, S. M., Water desalination using nanoporous single-layer graphene. *Nature nanotechnology* **2015,** *10* (5), 459-464.
27. Nan, H.; Wang, Z.; Wang, W.; Liang, Z.; Lu, Y.; Chen, Q.; He, D.; Tan, P.; Miao, F.; Wang, X.; Wang, J.; Ni, Z., Strong Photoluminescence Enhancement of MoS2 through Defect Engineering and Oxygen Bonding. *ACS Nano* **2014,** *8* (6), 5738-5745.
28. Li, L.; Yu, Y.; Ye, G. J.; Ge, Q.; Ou, X.; Wu, H.; Feng, D.; Chen, X. H.; Zhang, Y., Black phosphorus field-effect transistors. *Nat Nanotechnol* **2014,** *9* (5), 372-7.
29. Liu, H.; Neal, A. T.; Zhu, Z.; Luo, Z.; Xu, X.; Tománek, D.; Ye, P. D., Phosphorene: An Unexplored 2D Semiconductor with a High Hole Mobility. *ACS Nano* **2014,** *8* (4), 4033-4041.
30. Pang, J.; Bachmatiuk, A.; Yin, Y.; Trzebicka, B.; Zhao, L.; Fu, L.; Mendes, R. G.; Gemming, T.; Liu, Z.; Rummeli, M. H., Applications of Phosphorene and Black Phosphorus in Energy Conversion and Storage Devices. *Advanced Energy Materials* **2018,** *8* (8), 1702093.
31. Qiao, J.; Kong, X.; Hu, Z.-X.; Yang, F.; Ji, W., High-mobility transport anisotropy and linear dichroism in few-layer black phosphorus. *Nature Communications* **2014,** *5* (1), 4475.
32. Jiang, J.-W.; Park, H. S., Negative poisson's ratio in single-layer black phosphorus. *Nature Communications* **2014,** *5* (1), 4727.
33. Kou, L.; Frauenheim, T.; Chen, C., Phosphorene as a Superior Gas Sensor: Selective Adsorption and Distinct I-V Response. *J Phys Chem Lett* **2014,** *5* (15), 2675-81.
34. Xia, F.; Wang, H.; Jia, Y., Rediscovering black phosphorus as an anisotropic layered material for optoelectronics and electronics. *Nature Communications* **2014,** *5* (1), 4458.
35. Buscema, M.; Groenendijk, D. J.; Steele, G. A.; van der Zant, H. S.; Castellanos-Gomez, A., Photovoltaic effect in few-layer black phosphorus PN junctions defined by local electrostatic gating. *Nat Commun* **2014,** *5*, 4651.
36. Dai, J.; Zeng, X. C., Bilayer Phosphorene: Effect of Stacking Order on Bandgap and Its Potential Applications in Thin-Film Solar Cells. *The Journal of Physical Chemistry Letters* **2014,** *5* (7), 1289-1293.
37. Cai, Y.; Chen, S.; Gao, J.; Zhang, G.; Zhang, Y.-W., Evolution of intrinsic vacancies and prolonged lifetimes of vacancy clusters in black phosphorene. *Nanoscale* **2019,** *11* (43), 20987-20995.
38. Cai, Y.; Ke, Q.; Zhang, G.; Yakobson, B. I.; Zhang, Y.-W., Highly Itinerant Atomic Vacancies in Phosphorene. *Journal of the American Chemical Society* **2016,** *138* (32), 10199-10206.
39. Yao, F.; Cai, Y.; Xiao, Z.; Zhang, G.; Xie, R.-J.; Jin, C., In situ transmission electron microscopy study of the formation and migration of vacancy defects in atomically thin black phosphorus. *2D Materials* **2020,** *8* (2), 025004.
40. Hu, W.; Yang, J., Defects in Phosphorene. *The Journal of Physical Chemistry C* **2015,** *119* (35), 20474-20480.
41. Cai, Y.; Gao, J.; Chen, S.; Ke, Q.; Zhang, G.; Zhang, Y.-W., Design of Phosphorene for Hydrogen Evolution Performance Comparable to Platinum. *Chem. Mater.* **2019,** *31* (21), 8948-8956.
42. Zhu, M.; Kim, S.; Mao, L.; Fujitsuka, M.; Zhang, J.; Wang, X.; Majima, T., Metal-Free Photocatalyst for H(2) Evolution in Visible to Near-Infrared Region: Black Phosphorus/Graphitic Carbon Nitride. *J. Am. Chem. Soc.* **2017,** *139* (37), 13234-13242.

43. Atashzar, S. M.; Javadian, S.; Gharibi, H.; Rezaei, Z., Defective phosphorene as an anode material for high-performance Li-, Na-, and K-ion batteries: a first-principles study. *Nanoscale* **2020,** *12* (39), 20364-20373.
44. Ahmed, T.; Tahir, M.; Low, M. X.; Ren, Y.; Tawfik, S. A.; Mayes, E. L. H.; Kuriakose, S.; Nawaz, S.; Spencer, M. J. S.; Chen, H.; Bhaskaran, M.; Sriram, S.; Walia, S., Fully Light-Controlled Memory and Neuromorphic Computation in Layered Black Phosphorus. *Adv. Mater. n/a* (n/a), 2004207.
45. Ren, Y.; Hu, L.; Mao, J.-Y.; Yuan, J.; Zeng, Y.-J.; Ruan, S.; Yang, J.-Q.; Zhou, L.; Zhou, Y.; Han, S.-T., Phosphorene nano-heterostructure based memristors with broadband response synaptic plasticity. *Journal of Materials Chemistry C* **2018,** *6* (35), 9383-9393.
46. Kiraly, B.; Hauptmann, N.; Rudenko, A. N.; Katsnelson, M. I.; Khajetoorians, A. A., Probing Single Vacancies in Black Phosphorus at the Atomic Level. *Nano Lett.* **2017,** *17* (6), 3607-3612.
47. Chartier, A.; Meis, C.; Crocombette, J. P.; Weber, W. J.; Corrales, L. R., Molecular Dynamic Simulation of Disorder Induced Amorphization in Pyrochlore. *Phys. Rev. Lett.* **2005,** *94* (2), 025505.
48. Dholabhai, P. P.; Aguiar, J. A.; Misra, A.; Uberuaga, B. P., Defect interactions with stepped CeO2/SrTiO3 interfaces: Implications for radiation damage evolution and fast ion conduction. *The Journal of Chemical Physics* **2014,** *140* (19), 194701.
49. Narayanan, B.; Reimanis, I. E.; Huang, H.; Ciobanu, C. V., Radiation effects and tolerance mechanism in β-eucryptite. *J. Appl. Phys.* **2013,** *113* (3), 033504.
50. Trachenko, K., Understanding resistance to amorphization by radiation damage. *J. Phys.: Condens. Matter* **2004,** *16* (49), R1491-R1515.
51. Trachenko, K.; Dove, M. T.; Artacho, E.; Todorov, I. T.; Smith, W., Atomistic simulations of resistance to amorphization by radiation damage. *Physical Review B* **2006,** *73* (17), 174207.
52. Becquart, C. S.; Domain, C., Modeling Microstructure and Irradiation Effects. *Metallurgical and Materials Transactions A* **2011,** *42* (4), 852-870.
53. Lehtinen, O.; Kotakoski, J.; Krasheninnikov, A. V.; Tolvanen, A.; Nordlund, K.; Keinonen, J., Effects of ion bombardment on a two-dimensional target: Atomistic simulations of graphene irradiation. *Physical Review B* **2010,** *81* (15).
54. Ghaderzadeh, S.; Ladygin, V.; Ghorbani-Asl, M.; Hlawacek, G.; Schleberger, M.; Krasheninnikov, A. V., Freestanding and Supported MoS2 Monolayers under Cluster Irradiation: Insights from Molecular Dynamics Simulations. *ACS Applied Materials & Interfaces* **2020,** *12* (33), 37454-37463.
55. Xiao, H.; Shi, X.; Hao, F.; Liao, X.; Zhang, Y.; Chen, X., Development of a Transferable Reactive Force Field of P/H Systems: Application to the Chemical and Mechanical Properties of Phosphorene. *J. Phys. Chem. A* **2017,** *121* (32), 6135-6149.
56. Plimpton, S., Fast Parallel Algorithms for Short-Range Molecular Dynamics. *J. Comput. Phys.* **1995,** *117* (1), 1-19.
57. Ziegler, J. F.; Biersack, J. P., The stopping and range of ions in matter. In *Treatise on heavy-ion science*, Springer: 1985; pp 93-129.
58. Kretschmer, S.; Maslov, M.; Ghaderzadeh, S.; Ghorbani-Asl, M.; Hlawacek, G.; Krasheninnikov, A. V., Supported Two-Dimensional Materials under Ion Irradiation: The Substrate Governs Defect Production. *ACS Applied Materials & Interfaces* **2018,** *10* (36), 30827-30836.

59. Su, S.; Xue, J., Facile Fabrication of Subnanopores in Graphene under Ion Irradiation: Molecular Dynamics Simulations. *ACS Applied Materials & Interfaces* **2021,** *13* (10), 12366-12374.
60. Rumyantsev, A. V.; Borgardt, N. I.; Prikhodko, A. S.; Chaplygin, Y. A., Characterizing interface structure between crystalline and ion bombarded silicon by transmission electron microscopy and molecular dynamics simulations. *Applied Surface Science* **2021,** *540*, 148278.
61. Yoon, K.; Rahnamoun, A.; Swett, J. L.; Iberi, V.; Cullen, D. A.; Vlassiouk, I. V.; Belianinov, A.; Jesse, S.; Sang, X.; Ovchinnikova, O. S.; Rondinone, A. J.; Unocic, R. R.; van Duin, A. C. T., Atomistic-Scale Simulations of Defect Formation in Graphene under Noble Gas Ion Irradiation. *ACS Nano* **2016,** *10* (9), 8376-8384.
62. Senftle, T. P.; Hong, S.; Islam, M. M.; Kylasa, S. B.; Zheng, Y.; Shin, Y. K.; Junkermeier, C.; Engel-Herbert, R.; Janik, M. J.; Aktulga, H. M.; Verstraelen, T.; Grama, A.; van Duin, A. C. T., The ReaxFF reactive force-field: development, applications and future directions. *npj Computational Materials* **2016,** *2* (1), 15011.
63. van Duin, A. C. T.; Dasgupta, S.; Lorant, F.; Goddard, W. A., ReaxFF: A Reactive Force Field for Hydrocarbons. *The Journal of Physical Chemistry A* **2001,** *105* (41), 9396-9409.
64. van Duin, A. C. T.; Strachan, A.; Stewman, S.; Zhang, Q.; Xu, X.; Goddard, W. A., ReaxFFSiO Reactive Force Field for Silicon and Silicon Oxide Systems. *The Journal of Physical Chemistry A* **2003,** *107* (19), 3803-3811.
65. Narayanan, B.; van Duin, A. C. T.; Kappes, B. B.; Reimanis, I. E.; Ciobanu, C. V., A reactive force field for lithium–aluminum silicates with applications to eucryptite phases. *Modell. Simul. Mater. Sci. Eng.* **2011,** *20* (1), 015002.
66. Nordlund, K.; Ghaly, M.; Averback, R. S.; Caturla, M.; Diaz de la Rubia, T.; Tarus, J., Defect production in collision cascades in elemental semiconductors and fcc metals. *Physical Review B* **1998,** *57* (13), 7556-7570.
67. Björkas, C.; Nordlund, K., Comparative study of cascade damage in Fe simulated with recent potentials. *Nuclear Instruments and Methods in Physics Research Section B: Beam Interactions with Materials and Atoms* **2007,** *259* (2), 853-860.
68. Stoller, R. E.; Tamm, A.; Béland, L. K.; Samolyuk, G. D.; Stocks, G. M.; Caro, A.; Slipchenko, L. V.; Osetsky, Y. N.; Aabloo, A.; Klintenberg, M.; Wang, Y., Impact of Short-Range Forces on Defect Production from High-Energy Collisions. *Journal of Chemical Theory and Computation* **2016,** *12* (6), 2871-2879.
69. Grimme, S.; Ehrlich, S.; Goerigk, L., Effect of the damping function in dispersion corrected density functional theory. *Journal of Computational Chemistry* **2011,** *32* (7), 1456-1465.
70. Lehtinen, O.; Kotakoski, J.; Krasheninnikov, A. V.; Tolvanen, A.; Nordlund, K.; Keinonen, J., Effects of ion bombardment on a two-dimensional target: Atomistic simulations of graphene irradiation. *Physical Review B* **2010,** *81* (15), 153401.
71. Lehtinen, O.; Dumur, E.; Kotakoski, J.; Krasheninnikov, A. V.; Nordlund, K.; Keinonen, J., Production of defects in hexagonal boron nitride monolayer under ion irradiation. *Nuclear Instruments and Methods in Physics Research Section B: Beam Interactions with Materials and Atoms* **2011,** *269* (11), 1327-1331.
72. Taioli, S., Enabling Materials By Dimensionality: From 0D to 3D Carbon-Based Nanostructures. In *Theoretical Chemistry for Advanced Nanomaterials: Functional Analysis by Computation and Experiment*, Onishi, T., Ed. Springer Singapore: Singapore, 2020; pp 135-200.
73. Qiao, J.; Kong, X.; Hu, Z.-X.; Yang, F.; Ji, W., High-mobility transport anisotropy and linear dichroism in few-layer black phosphorus. *Nature communications* **2014,** *5* (1), 1-7.

74. Yu, W.; Zhu, Z.; Niu, C.-Y.; Li, C.; Cho, J.-H.; Jia, Y., Anomalous doping effect in black phosphorene using first-principles calculations. *Physical Chemistry Chemical Physics* **2015,** *17* (25), 16351-16358.
75. Cherukara, M.; Narayanan, B.; Kinaci, A.; Sasikumar, K.; Gray, S.; Chan, M.; Sankaranarayanan, S., Ab Initio-Based Bond Order Potential to Investigate Low Thermal Conductivity of Stanene Nanostructures. *Journal of Physical Chemistry Letters* **2016,** *7* (19), 3752-3759.
76. Li, Z.; Chen, F., Ion beam modification of two-dimensional materials: Characterization, properties, and applications. *Applied Physics Reviews* **2017,** *4* (1), 011103.
77. Chen, Y.; Shi, X.; Li, M.; Liu, Y.; Xiao, H.; Chen, X., Strain and defect engineering on phase transition of monolayer black phosphorene. *Physical Chemistry Chemical Physics* **2018,** *20* (34), 21832-21843.
78. Carvalho, A.; Wang, M.; Zhu, X.; Rodin, A. S.; Su, H.; Castro Neto, A. H., Phosphorene: from theory to applications. *Nature Reviews Materials* **2016,** *1* (11).
79. Osman, R.; Coffey, P.; Van Wazer, J. R., Use of pseudopotential theory to study molecular structure. II. NOCOR (neglect of core orbitals) calculation of the P4 and P2 molecules and their interconversion. *Inorganic Chemistry* **1976,** *15* (2), 287-292.
80. Pauling, L.; Simonetta, M., Bond orbitals and bond energy in elementary phosphorus. *The Journal of Chemical Physics* **1952,** *20* (1), 29-34.
81. Liu, J.; Guo, Y.; Zhang, S.; Wang, Q.; Kawazoe, Y.; Jena, P., New Phosphorene Allotropes Containing Ridges with 2- and 4-Coordination. *The Journal of Physical Chemistry C* **2015,** *119* (43), 24674-24680.
82. Ester, M.; Kriegel, H.-P.; Sander, J.; Xu, X., A density-based algorithm for discovering clusters in large spatial databases with noise. In *Proceedings of the Second International Conference on Knowledge Discovery and Data Mining*, AAAI Press: Portland, Oregon, 1996; pp 226–231.
83. Liu, Y.; Xu, F.; Zhang, Z.; Penev, E. S.; Yakobson, B. I., Two-dimensional mono-elemental semiconductor with electronically inactive defects: the case of phosphorus. *Nano Lett.* **2014,** *14* (12), 6782-6.
84. Hu, T.; Dong, J., Geometric and electronic structures of mono- and di-vacancies in phosphorene. *Nanotechnology* **2015,** *26* (6), 065705.
85. Gao, J.; Zhang, J.; Liu, H.; Zhang, Q.; Zhao, J., Structures, mobilities, electronic and magnetic properties of point defects in silicene. *Nanoscale* **2013,** *5* (20), 9785-92.
86. Gaberle, J.; Shluger, A. L., Structure and properties of intrinsic and extrinsic defects in black phosphorus. *Nanoscale* **2018,** *10* (41), 19536-19546.
87. Umar Farooq, M.; Hashmi, A.; Hong, J., Anisotropic bias dependent transport property of defective phosphorene layer. *Scientific Reports* **2015,** *5* (1), 12482.
88. Srivastava, P.; Hembram, K. P. S. S.; Mizuseki, H.; Lee, K.-R.; Han, S. S.; Kim, S., Tuning the Electronic and Magnetic Properties of Phosphorene by Vacancies and Adatoms. *The Journal of Physical Chemistry C* **2015,** *119* (12), 6530-6538.
89. Cupo, A.; Masih Das, P.; Chien, C.-C.; Danda, G.; Kharche, N.; Tristant, D.; Drndić, M.; Meunier, V., Periodic Arrays of Phosphorene Nanopores as Antidot Lattices with Tunable Properties. *ACS Nano* **2017,** *11* (7), 7494-7507.